Article

Hydroxyapatite Incorporated with Fe_3O_4@MCM-41 Core−Shell: A Promising Nanocomposite for Teriparatide Delivery in Bone Tissue Regeneration

Hamid Reza Hosseini, Majid Abdouss,* and Mostafa Golshekan

Read Online

ACCESS | Metrics & More | Article Recommendations | SI Supporting Information

ABSTRACT: This article presents a comprehensive study of the development of a novel nanocomposite comprising core−shell Fe_3O_4@MCM-41 with superparamagnetic properties and hydroxyapatite (HAp). The nanocomposite serves as a pH-responsive nanocarrier, offering an efficient injectable dosage for teriparatide (PTH (1−34)) delivery. The aim is to address the limitations associated with drug-induced side effects, precautionary measures, and frequent injections. The nanocomposites, as prepared, were characterized using techniques including X-ray diffraction, Fourier transform infrared, zeta potential, dynamic light scattering, VSM, scanning electron microscopy, and transmission electron microscopy. The nanocomposites' average crystallite diameter was determined to be 27 ± 5 nm. The hydrodynamic size of the PTH (1−34)-loaded nanocarrier ranged from 357 to 495 nm, with a surface charge of −33 mV. The entrapment and loading efficiencies were determined to be 73% and 31%, respectively. All of these findings collectively affirm successful fabrication. Additionally, in vivo medication delivery was investigated using the HPLC method, mirroring the in vitro tests. Utilizing the dialysis approach, we demonstrated sustained-release behavior. PTH (1−34) diffusion increased as the pH decreased from 7.4 to 5.6. After 24 h, drug release was higher at acidic pH (88%) compared to normal pH (43%). The biocompatibility of the PTH (1−34)-loaded nanocarrier was assessed using the MTT assay employing the NIH3T3 and HEK-293 cell lines. The results demonstrated that the nanocarrier not only exhibited nontoxicity but also promoted cell proliferation and differentiation. In the in vivo test, the drug concentration reached 505 μg within 30 min of exposure to the magnetic field. Based on these findings, the Fe_3O_4@MCM-41/HAp/PTH (1−34) nanocomposite, in combination with a magnetic field, offers an efficient and biocompatible approach to enhance the therapeutic effect of osteogenesis and overcome drug limitations.
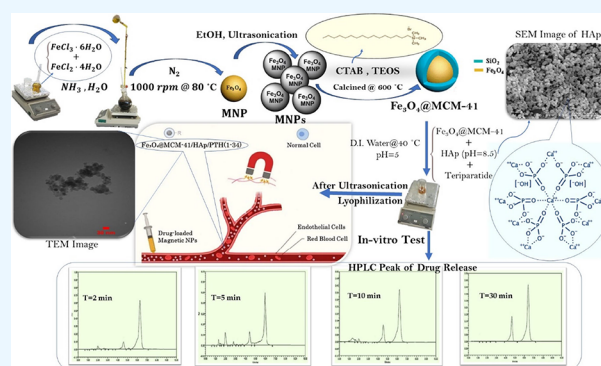
1. INTRODUCTION

Bone fractures, especially in the spine and long bones, have a significant impact on patient well-being and are associated with high mortality rates.[1−4] Challenges in treatment include instability, low drug effectiveness due to poor bioavailability and short half-lives, and side effects.[5] Emerging solutions include innovative therapeutic agents,[6] technologies like 3D printing and bone scaffolding,[7,8] finite element software for surgeries,[9] methods to enhance bone density,[10,11] targeted drug delivery,[12] and combined treatments.[6]

Given bones' widespread distribution,[13] systemic therapies require sufficient blood concentration for peripheral effects, leading to severe side effects and a limited bone disease treatment range. Delivering protein and peptide drugs is challenging due to size and solubility.[14] Therefore, innovative drug delivery strategies are vital.

Teriparatide [PTH (1−34)], a synthetic parathyroid hormone analogue, aids bone healing. It regulates the phosphorus and calcium balance, stimulating bone responses at low concentrations. Research shows its benefits in animal fracture models, enhancing callus mineralization, production, remodeling, and density.[15] PTH (1−34) improves post-operative outcomes and fracture healing.[15] It is FDA-approved for osteoporosis along with abaloparatide.[16,17] High doses relate to side effects and osteosarcoma risk.[18−21] It is administered cautiously to those with kidney, hypercalcemia, or cardiovascular issues.[22] Intermittent use over two years poses challenges.[14]

Hydroxyapatite (HAp), a calcium phosphate variant, integrates fluoride, sodium, and magnesium ions into the bone mineral structure. Over the past two decades, it gained

medical attention for its unique properties.[23] HAp boasts osteoconductivity, high biocompatibility, ideal for bone grafts, scaffolds, implants, coatings, and drug delivery.[24,25] It enhances biological molecule conductivity, has low solubility, adjustable porosity, surface area, and characteristics, suitable for drug carriers via injection or surgery.[26−28] HAp aids drug delivery to damaged bone and cancer areas, with gradual drug release.[29] Except for small hydrophilic molecules, HAp loads various molecules and drugs. Multilayer structures enable loading multiple drugs onto apatite.[30] Studies have indicated that temperature and the sol−gel-derived synthesis method have a direct impact on the crystal particle size, properties, and purity of HAp nanoparticles[31] that influence their suitability for bone tissue engineering applications.

Magnetic materials are gaining attention in medicine, biology, and pharmaceuticals. Among them,[32] Fe_3O_4 NPs stand out due to their superparamagnetic properties, low Curie temperature, nontoxicity, and biocompatibility.[33−37] Fe_3O_4 NPs can be guided to target tissues using external magnetic fields, reducing adverse effects and allowing lower drug dosages.[38] Coating with organic or inorganic materials enhances their biocompatibility.[39]

Protective agents are vital to prevent clotting and oxidation of magnetite nanoparticles, ensuring colloidal stability.[40] Coating these nanoparticles controls drug loading, delivery, and release, reducing toxicity, and enhancing biocompatibility.[41] Silica coating, common in catalysis and drug delivery, safeguards magnetite nanoparticles from aggregation and improves properties.[42−46] Mesoporous silicates offer benefits like large surface area, varied pore sizes, and stability.[45,47] Silica supports can be chemically modified with functional groups.[48−50] Mobil Composition of Matter No. 41 (MCM-41) has been studied as a carrier for poorly soluble medications.[51−53] Research also emphasizes simpler, efficient synthetic methods for controlled-release drug delivery systems.[42,48,54−57]

Recently, several innovative nanocomposite systems have emerged for cell-specific targeting of bone, enhancing drug solubility, improving drug stability, and preventing drug degradation, thereby enabling drugs to reach their intended locations without being eliminated in the systemic circulation.[58,59] This study introduces a novel nanocomposite, Fe_3O_4@MCM-41/HAp/PTH (1−34), combining HAp synthesized by the sol−gel method and mesoporous Fe_3O_4@MCM-41 with significant individual effects on bone tissue engineering as mentioned by the literature. However, there is limited research on the use of Fe_3O_4 NPs@SiO_2/HAp composites as nanocarriers[60,61] which had problems in the synthesis method, such as high pressure and temperature for several hours, as well as the impossibility of simplicity.

In this study, the emphasis was on designing and producing a controllable nanocomposite capable of carrying drugs and enabling controlled release for bone healing, which is characterized by core−shell structures. By employing this technique, it was possible to enhance bone tissue repair while mitigating the systemic side effects and limitations associated with the drug. Consequently, a specialized and targeted drug delivery system was established. To evaluate the effectiveness of the composite, we performed an MTT assay using the mouse embryonic NIH3T3 fibroblast cell line as well as immortalized human embryonic kidney cells (HEK-293). Subsequently, in vitro testing was carried out to assess drug release, and in vivo experiments were conducted to examine drug delivery.

2. EXPERIMENTAL SECTION

2.1. Materials and Apparatus. All chemicals used in this study, including tetraethyl orthosilicate (TEOS), cetyltrimethylammonium bromide (CTAB), $FeCl_3·6H_2O$, $FeCl_2·4H_2O$, NH_3, NaOH, NaF, and HCl, were of analytical grade and obtained from Merck. Pure deionized water, produced using double reverse osmosis technology with a conductivity of 0.0 micro siemens, was utilized. High-purity hydroxyapatite (HAp) was purchased from Nic Ceram, and teriparatide [PTH (1−34)] was obtained under the brand name Cinnopar from Cinnagen. A dialysis bag with a 12 kDa cutoff and trypsin were employed for the release process assessment. Several instrumental techniques were employed to characterize the produced nanocomposite, including Shimadzu Fourier transform infrared (FTIR) spectroscopy (Japan, model 470) in the range of 400−4000 $cm^{−1}$, X-ray diffraction (XRD) using the X Thermo Scientific ARL EQUINOX 3000 instrument, vibrating sample magnetometry (VSM), dynamic light scattering (DLS) using the Malvern Zetasizer ZS (Malvern, UK), scanning electron microscopy (SEM), and PHILIPS transmission electron microscopy (TEM) with the CM10 HT 100 kV model. The MTT assay was performed to evaluate the cell cytotoxicity. Chemical mixing was conducted using a universal ultrasonic device (DSA100-SK2), pH adjustments were made using a digital Jenway pH meter equipped with a combined glass-calomel electrode, freeze-drying was carried out using a Christ lyophilization system (Germany), Teflon-lined hydrothermal autoclave (300 mL, Safe Temp −200 °C), and a strong magnet (Nd−Fe−B, 1 T) was employed to separate the solid magnetic phase from the solution.

2.2. Synthesis of Fe_3O_4 Magnetite Nanoparticles. The synthesis of Fe_3O_4 nanoparticles, following the precipitated method,[62,63] was carried out in accordance with our previous work. To prepare the stock solution of ferrous and ferric chloride, 6.3 g of $FeCl_3·6H_2O$, 4.0 g of $FeCl_2·4H_2O$, and 1.7 mL of HCl (12 mol $L^{−1}$) were dissolved in 50 mL of deionized water in a beaker. The solution was then degassed using argon gas and heated to 80 °C in a reactor. Concurrently, 250 mL of 1.5 mol. $L^{−1}$ ammonia solution was gradually added to the solution while being shielded with argon gas and vigorously stirred at 1000 rpm. Throughout this process, the solution temperature was maintained at 80 °C, and argon gas was continuously introduced to prevent oxygen penetration. The resulting Fe_3O_4 nanoparticles were collected by employing an external magnet, followed by four rinses with 500 mL of doubly distilled water and ethanol (50:50). In conclusion, the Fe_3O_4 magnetite nanoparticles (MNPs) obtained were resuspended in 500 mL of degassed deionized water, leading to an achieved concentration of 6.2 mg $mL^{−1}$ for the Fe_3O_4 MNPs. The precipitate was subsequently dried overnight at 50 °C.[64]

2.3. Synthesis of Fe_3O_4@MCM-41. To achieve a standard core−shell structure, it is crucial to begin by selecting a low concentration of magnetic nanoparticles and subjecting them to ultrasound. This step ensures that polyunsaturated iron oxide does not form within the silica shell. Once the fresh synthesis is completed, immediate coating of Fe_3O_4 MNPs with MCM-41 is performed to prevent oxidation. During the coating process, Fe_3O_4 MNPs (1.5 g) and 5 mL (25%) of ammonia solution were mixed with 50 mL of distilled water in

a glass reactor. Following this, the mixture was sonicated for 2 min at 40 °C. Next, 10 mL of TEOS solution was gradually added to the mixture. The solution was stirred on a magnetic stirrer at a temperature of 40 °C for 1 h. After that, 0.9 g of NaOH (0.1 mol L^{-1}) and 0.19 g of NaF were added and stirred for an additional hour. Subsequently, 4 g of the CTAB surfactant, serving as a template, was slowly introduced and stirred for 2.5 h. The resulting combination was then subjected to hydrothermal processing in an autoclave for 48 h to generate a core−shell nanocomposite. Following hydrothermal processing, the nanocomposite underwent multiple rinses with a 50:50 ethanol/deionized water solution. Finally, the separated precipitate was calcined in a furnace at a temperature of 600 °C, resulting in the formation of the mesoporous Fe$_3$O$_4$@MCM-41 composite.[46,63,65,66]

2.4. Synthesis of Fe$_3$O$_4$@MCM-41/HAp. The synthesis of Fe$_3$O$_4$@MCM-41/HAp was carried out through a three-step process. In the first step, 0.7 g of Fe$_3$O$_4$@MCM-41 was dispersed in 10 mL of deionized water (pH 5, adjusted with HCl) and heated on a stirrer at 40 °C for 60 min. Moving on to step 2, HAp was activated by adding it to 10 mL of deionized water with a pH of 8.5 (adjusted with NaOH), using a weight ratio of HAp to Fe$_3$O$_4$@MCM-41 of 1:5. The mixture was stirred at 40 °C for one h, followed by filtration and drying of the solid phase. In the final step, activated HAp obtained from step 2 was gradually added to the solution prepared in step 1. The resulting mixture was stirred for 30 min at 40 °C using an ultrasonic device. Subsequently, the precipitate was separated by using an external magnet and dehydrated in an 80 °C furnace.

2.5. Acquisition of Fe$_3$O$_4$@MCM-41/HAp/PTH (1−34) through Fabrication. To obtain Fe$_3$O$_4$@MCM-41/HAp/PTH (1−34), 10 mL of distilled water was combined with 0.1 g of the nanocomposite. The mixture was then subjected to ultrasonic treatment in a tub for 30 min to ensure the uniform distribution of the nanocomposite. Subsequently, the nanocomposite solution was transferred to a stirrer and 1 mL of the drug, with a concentration of 300 μg/mL, was added to it. The mixture was allowed to stir for 3 h. Following this, the solution was subjected to centrifugation for 10 min to remove any unbound drug. Finally, the drug-loaded nanocomposite was freeze-dried.

2.6. Determination of Encapsulation Efficiency (EE) and Drug Loading (DL). To evaluate the effectiveness of drug loading and encapsulation, 1 mg of lyophilized Fe$_3$O$_4$@MCM-41/HAp/PTH (1−34) nanocarrier was dissolved in 1 mL of phosphate-buffered saline (PBS). The nanocarriers were then mixed with 1 mL of ethyl acetate to extract both the nanocomposite and the drug, and eqs 1 and 2 were employed to calculate the percentage of PTH (1−34) encapsulation and loading efficiency, respectively[64]:

$$\text{Encapsulation Efficiency (\%)} = \frac{(\text{total amount of PTH}) - (\text{Free amount of PTH})}{\text{total amount of PTH}} \times 100 \tag{1}$$

$$\text{Loading Efficiency (\%)} = \frac{(\text{total amount of PTH}) - (\text{Free amount of PTH})}{\text{total amount of Nanocomposite}} \times 100 \tag{2}$$

2.7. Research on In Vitro Drug Emission. The emission of PTH (1−34) from the nanocarrier was investigated by using the dialysis method. The experiments were conducted by submerging a dialysis membrane containing the drug-loaded nanocomposite in phosphate buffered saltwater at 37 °C, with pH levels of 7.4 and 5.6. Samples were collected at regular intervals of 0, 1, 2, 3, 6, 12, and 24 h, and 1 mL of the surrounding PBS solution was extracted each time before adding fresh buffer. The release medium was then analyzed using high-performance liquid chromatography (HPLC) to measure the concentration of PTH (1−34), following the chromatographic conditions described in previous studies.[14,67] Each experiment was repeated three times, and the release percentage of PTH (1−34) from the nanocomposite at pH values of 5.6 and 7.4 was evaluated. Statistical analysis (ANOVA) was performed to verify the pH-responsive release behavior of the synthesized platform:

$$\begin{aligned} &\text{PTH}(1-34) \text{ released (\%)} \\ &= \frac{\text{Amount of PTH released at time "t"}}{\text{Amount of PTH loaded in the nanocomposite}} \\ &\quad \times 100 \end{aligned} \tag{3}$$

2.8. Cell Culture. To assess the impact of insufficient endogenous PTH on renal calcium reabsorption, immortalized human embryonic kidney cells (HEK-293) and a mouse embryo fibroblast cell line (NIH3T3) were utilized for the cytotoxicity assay.

2.9. Cytotoxicity Assay. The cytotoxicity of various substances, including free PTH (1−34), PTH (1−34)-loaded nanocomposite Fe$_3$O$_4$@MCM-41/HAp/PTH (1−34), Fe$_3$O$_4$ NPs, Fe$_3$O$_4$@MCM-41, and Fe$_3$O$_4$@MCM-41/HAp, was assessed using the MTT assay (3-[4,5-dimethylthiazol-2-yl]-2,5-diphenyl tetrazolium bromide). The assessment followed the instructions outlined in previous studies.[17,68] Cell viability was calculated using eq 4.

$$\text{Cell Viability (\%)} = \frac{\text{Sample absorption}}{\text{Control absorption}} \times 100 \tag{4}$$

2.10. In Vivo Study. *2.10.1. Methods.* To examine the effectiveness of the synthesized nanodrug inside a living organism (in vivo), rats were employed as experimental subjects. The research study was conducted with the approval ID: IR.IAU.REC.1401.034 was obtained from the Research Ethics Committee's certification (Research Ethics Committees of Islamic Azad University-Central Tehran Branch). All experimental procedures were authorized by the licensing committee, and we affirm that they were carried out in strict adherence to the applicable guidelines and regulations. The reporting in this article adheres to the recommendations outlined in the ARRIVE guidelines. The rats used in the study were acquired from a designated animal facility at Kermanshah University and maintained under controlled conditions to ensure they were pathogen-free. All handling procedures were conducted in compliance with the European Convention for the Protection of Vertebrate Animals Used for Experimental and Other Scientific Purposes (ETS 123). The animals were housed at a constant temperature of 21 °C and a humidity level of 50−60%. They were provided with ad libitum access to drinking water and normal food. The experiments were carried out using rats with an average weight of 260 g. An anesthetic
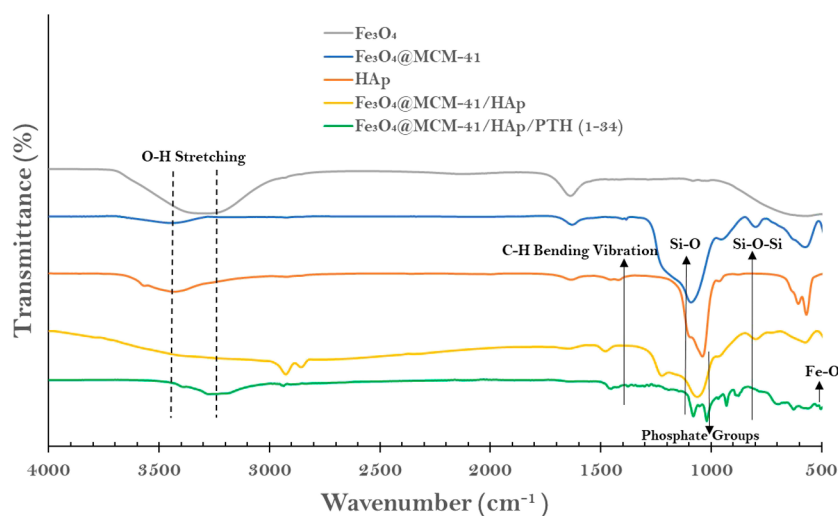
Figure 1. FT-IR spectra of Fe_3O_4 NPs, Fe_3O_4@MCM-41, HAp, Fe_3O_4@MCM-41/HAp, and Fe_3O_4@MCM-41/HAp/PTH (1−34) nanocarriers, showing the range of chemical bonds.

agent, ketamine/xylazine, was administered during the experimental procedures.

2.10.2. Assessment of In Vivo Drug Release. To assess in vivo drug release, two groups of 8 animals each were utilized, with each group consisting of 4 males and 4 females. Initially, the mice were anesthetized, following which 10 mg of the synthesized nanodrug was administered through the left leg artery in the first group. Simultaneously, an equivalent amount of PTH (1−34) weighing 0.29 mg, which matches the drug content in the nanocomposite, was injected into the second group.

Subsequent to the injection, the animals in the first group were subjected to a magnetic field (1 T) originating from the right-hand region. Additionally, for validation purposes, the aforementioned procedure was replicated by using a group of 16 animals without the application of a magnetic field, representing the direct administration of medication. Notably, the concentration of the teriparatide injection remained consistent across both groups.

2.10.3. Evaluation of PTH (1−34) Levels in Bone Tissue. Following the in vivo examination of the drug and adherence to the designated time intervals, the animal was promptly euthanized and the bone from its right hand was isolated and weighed. Subsequently, the entire tissue was subjected to freeze-drying and pulverized into a powder (utilizing a water/ethanol solvent in a 1:1 ratio). Drug extraction was performed, and the obtained sample was analyzed by using the HPLC technique. The Supporting Information contains the HPLC data for reference.

3. RESULTS AND DISCUSSION

3.1. Characterization of the Synthesized Magnetic Nanocomposite. The Fe_3O_4@MCM-41/HAp/PTH (1−34) nanocomposite underwent evaluation using various techniques, including FT-IR, XRD, VSM, DLS, zeta potential, SEM, and TEM. The objective was to assess the chemical bonds and functional groups of the produced nanoparticles by employing FT-IR. XRD analysis was utilized to identify the crystalline phase present in the materials and ascertain the composition, physicochemical properties, minerals, and polymers. VSM measurement served to determine the magnetic order and potential interaction effects among nanoparticles due to their

HAp, size, and surface characteristics. Size distribution of the nanocomposites and colloidal stability were investigated through DLS analysis. Zeta potential was measured to evaluate the stability of the electrostatic field and sample dispersion. SEM was employed to test and analyze the morphology of nanostructures and identify chemical compounds, while TEM was used to determine the structure and morphology, symmetry, orientation, and crystalline defects of the materials.

3.1.1. Exploring Functional Groups and Analyzing Organic and Inorganic Compounds. Figure 1 illustrates the FT-IR bands of different constituents within the nanocomposite, providing evidence of the chemical structure of the produced nanocomposites. Wide peaks ranging from 3250 to 3450 cm^{-1} were observed, corresponding to the O−H bending vibrations of surface −OH and absorbed water. Additionally, at approximately 1600 cm^{-1}, there were expanding oscillations of these bonds.[69] All the mesoporous compounds exhibited characteristic absorptions of the MCM-41 structure at 475, 820, and 1089 cm^{-1}, which arise from symmetric and asymmetric bending and stretching modes of Si−O−Si bonds.[70] The wave numbers 563 and 503 cm^{-1} were associated with Fe−O vibrations in tetrahedral and octahedral sites, respectively. Furthermore, a prominent peak at 1100 cm^{-1} confirmed the Si−O stretching vibration in the amorphous silica shell, validating the presence of Fe_3O_4 as the magnetic core. Comparisons of the spectra for Fe_3O_4@MCM-41, Fe_3O_4@MCM-41/HAp, and HAp showed no discernible differences. Moreover, in the case of the Fe_3O_4@MCM-41/HAp/PTH (1−34) nanocarrier, the spectra indicated the presence of silicon dioxide resulting from the formation of the Fe−O−Si bond through TEOS, as well as the presence of hydroxyl groups. The spectra also displayed the C−H stretching and bending vibrations of terminal-type trialkoxy organosilanes $(R_1O)_3SiR_2$ coherent of TEOS at 2800−3000 and 1400 cm^{-1}.[63] The high-intensity zones at around 1000 cm^{-1} represented the stretching vibration of the PO_4^{3-} groups in the FT-IR spectra of Fe_3O_4@MCM-41/HAp/ and Fe_3O_4@MCM-41/HAp/PTH (1−34) nanocarriers. The FT-IR spectra revealed identical spectra for both nanocomposites Fe_3O_4 and Fe_3O_4@MCM-41, confirming their successful fabrication. Additionally, in Figure 1, the presence of PTH (1−34) was evident through a strong amide connection
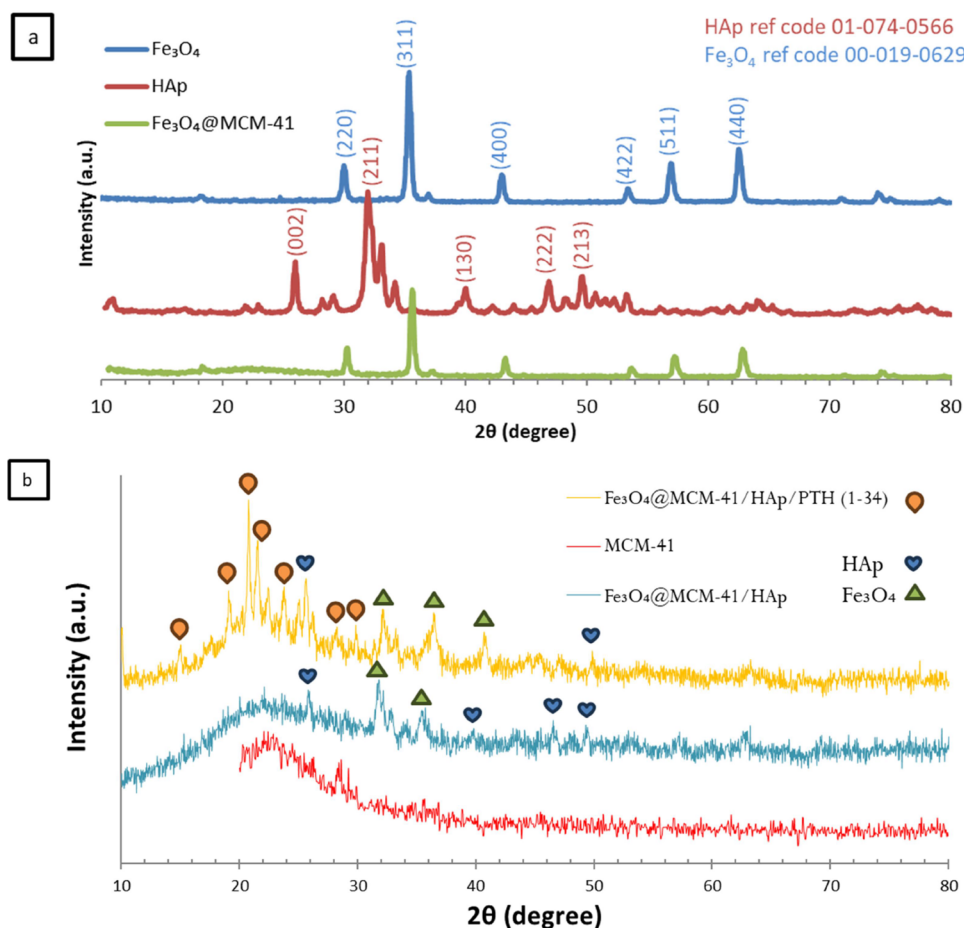
Figure 2. (a); XRD patterns, qualitative and quantitative analysis of Fe_3O_4, Fe_3O_4@MCM-41, HAp, (b); X-ray diffraction patterns of MCM-41, Fe_3O_4@MCM-41/HAp, and Fe_3O_4@MCM-41/HAp/PTH (1−34) nanocarriers.
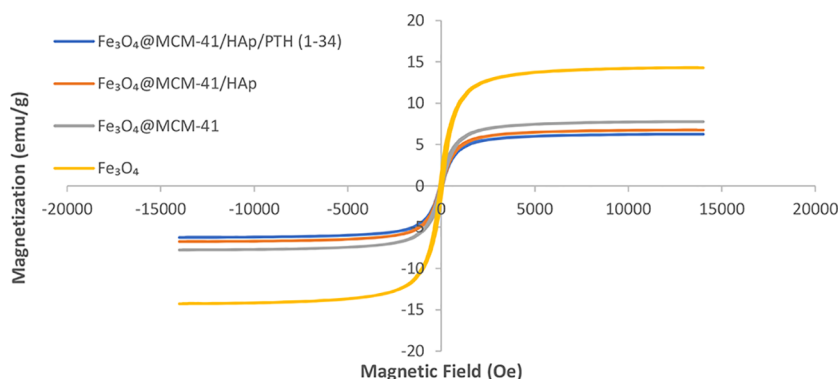

Figure 3. VSM hysteresis of Fe_3O_4, Fe_3O_4@MCM-41, Fe_3O_4@MCM-41/HAp, and Fe_3O_4@MCM-41/HAp/PTH (1−34) nanocarriers.

with the C=O group located at 1492 cm^{-1}. The interaction between the N−H bending and the C−N stretching of the C−N−H group resulted in the stretching bond at 1435 cm^{-1}.[14]

3.1.2. Study of Crystalline Structures. The X-ray diffraction (XRD) patterns of mesoporous Fe_3O_4 nanoparticles (NPs) exhibited peaks corresponding to both the mesoporous structures and Fe_3O_4 NPs. Figure 2 shows the XRD pattern, indicating that the attractive crystal structure remains unchanged throughout the synthesis process. Additionally, it has been confirmed that Fe_3O_4 nanoparticles are present in the entire sample. Moreover, the diffraction peak at $2\theta = \sim23°$ can be attributed to the SiO_2 amorphous Fe_3O_4@MCM-41. The

Fe_3O_4 NP patterns display peaks at $2\theta = 18−70$ (18.24, 24.16, 30.09, 35.32, 36.96, 43.06, 53.40, 56.96, 62.51, and 65.77), which are identical to those of the pure magnetite with a spherical structure. The XRD pattern of Fe_3O_4 NPs corresponds to the spinal magnetite pattern described by the Joint Committee on Powder Diffraction Standards (JCPDS file No. 19-06 29).

As shown in Figure 2a, it can be observed that both single-phase compounds, Fe_3O_4 NPs and HAp, were successfully synthesized using the reference codes 00-019-0629 and 01-074-0566, respectively.

The XRD data enabled the calculation of the nano-composites' crystallite diameter (D_c) using the Debye Scherer equation provided below (eq 5), where "λ" represents the wavelength of the X-ray source employed, "K" denotes the shape factor (typically 0.9), "β" signifies the breadth of the observed d fraction line at its half intensity maximum, and "θ" diffraction angle.[60,71,72]

$$D_c = \frac{k\lambda}{\beta \cos \theta} \tag{5}$$

The average size of the nanocomposites' crystallite diameter was 27 ± 5 nm.

3.1.3. Study of Magnetic Properties. The magnetic properties of the different layers in the nanocomposite were evaluated by using a vibrating sample magnetometer at room temperature. As depicted in Figure 3, the saturated magnetization and superparamagnetic samples were investigated. Among the components, Fe_3O_4 NPs exhibited the highest saturated magnetization value (M_s = 14.28 emu/g), while Fe_3O_4@MCM-41, Fe_3O_4@MCM-41/HAp, and Fe_3O_4@MCM-41/HAp/PTH (1−34) nanocarriers displayed Ms values of 7.77, 6.76, and 6.26 emu/g, respectively. The saturation magnetization is likely reduced due to the presence of silica and HAp shells coated on the Fe_3O_4 nanoparticles. The nonmagnetic HAp/PTH (1−34) moieties were loaded onto the surface of the magnetic support, providing a reasonable explanation for the lower Ms value of the final nanocomposite. However, it is important to note that the actual Ms value of the nanocomposite remained sufficiently high to enable magnetic separation using a standard magnet.[73] Consequently, the distance between Fe_3O_4 nanoparticles is increased, and the interaction strength is decreased.[45]

3.1.4. Microstructural Analysis. Figure 4 presents the SEM and transmission electron microscopy micrographs of the
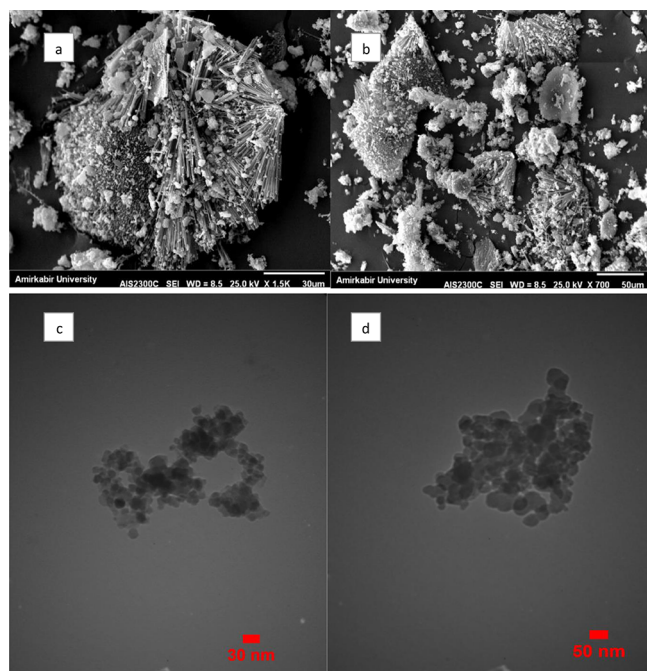
synthesized Fe_3O_4@MCM-41/HAp/PTH (1−34) mesoporous magnetite nanocomposite (MMNPs). Upon examining the SEM images, it was observed that the HAp crystals exhibited a uniform, rodlike shape, albeit with varying sizes. Specifically, the crystal size of HAp ranged from submicron to micron levels, with lengths measuring between 400 nm to 3 μm and widths ranging from 50 to 100 nm.[74] The addition of HAp to the surface of the Fe_3O_4@MCM-41 microspheres led to noticeable aggregation.

TEM analysis was conducted by using two-scale bars. The nanocarriers displayed a spherical morphology with a homogeneous and uniform distribution, indicating the successful synthesis of the nanocarriers. According to the TEM images, the nanocarriers exhibited sizes ranging from 15 to 55 nm. The images also revealed the presence of an MCM-41/HAp shell encompassing the Fe_3O_4 nanoparticles, and distinct core−shell structures were clearly distinguishable, validating the desired sample outcome. The final nanoparticles exhibited an organic shell with a brighter hue, while the inorganic core (Fe_3O_4 NPs) appeared denser and blacker.[75] The diameter of the spherical nanocarriers observed in the TEM images corresponded to the crystal size determined by using the Scherrer equation. Both TEM and SEM images unveiled the aggregation of numerous ultrafine particles with diameters of approximately 15 nm.

3.1.5. Zeta Potential and DLS. Figure 5a illustrates the zeta potential values of the components of the Fe_3O_4@MCM-41/
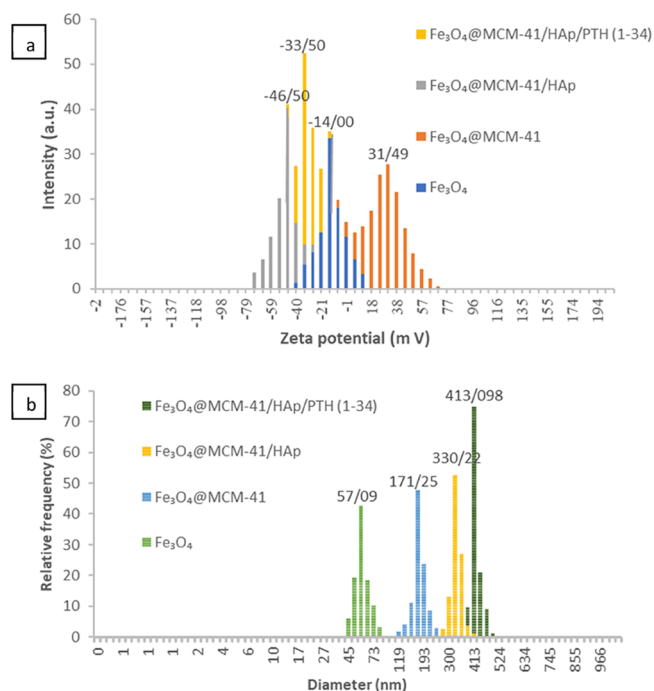
Figure 4. SEM and TEM images of the Fe_3O_4@MCM-41/HAp/PTH (1−34) nanocarrier and its size distribution: (a,b) 30 and 50 μm scalebar, respectively, related to SEM images and (c,d) 30 and 50 nm scalebar, respectively, related to TEM images.

Figure 5. (a) Zeta potential and (b) the particle size distribution of Fe_3O_4 NPs, Fe_3O_4@MCM-41, Fe_3O_4@MCM-41/HAp, Fe_3O_4@MCM-41/HAp/PTH (1−34) nanocarriers.

HAp/PTH (1−34) nanocomposite, determined through laser Doppler electrophoresis over a voltage range of ± 200 mV. The purpose of the zeta potential test was to investigate any surface charge changes that occurred during the fabrication of the nanocomposite. Initially, the zeta potential value of Fe_3O_4 nanoparticles (NPs) was measured at −14 mV. However, with the introduction of a silica coating through the silane agent and

CTAB cationic surfactant, the surface charge increased to +32 mV, indicating the successful implementation of the covalent surface modification method.

The surface charge of Fe_3O_4@MCM-41/HAp, exhibited a negative value of −46 mV, attributed to the high negative charge of the phosphate ion. For the Fe_3O_4@MCM-41/HAp/ PTH (1−34) nanocomposite, this value reduced to −33 mV. This decrease in surface charge is an indicator of the excellent stability of the nanocarriers, as particles with higher surface charges tend to be more stable.[76,77] The negative charge of HAp leads to electrostatic interactions among the particles, facilitating the dispersion of positively charged particles in the system. The drug molecules establish covalent bonds directly with the hydroxyl groups of HAp, with electrostatic and hydrogen bonds playing significant roles in this process.[78] Based on the results, the covalent functionalization procedure has proven to be effective, as intended.

To determine the particle sizes and their distribution, DLS analysis was conducted using the Malvern Nano-Zetasizer ZS 90 (UK) with a scattering angle of 176.1, following our previous methodology.[79] The reported diameter represents the particle size (z-average), which is an intensity-weighted average of two observations with an estimated accuracy of no more than 2%. Figure 5b illustrates the particle size distribution of the colloids. The Fe_3O_4 NPs, Fe_3O_4@MCM-41, Fe_3O_4@ MCM-41/HAp, and Fe_3O_4@MCM-41/HAp/PTH (1−34) nanocomposites had average diameters of approximately 57, 171, 330, and 413 nm, respectively. As expected, the diameter of the nanocomposite layers increased during the fabrication process due to the successive coating of each layer, which aligns well with the findings from SEM analysis. For instance, the SEM-derived diameter range of the Fe_3O_4@MCM-41/ HAp/PTH (1−34) nanocomposite was between 357 and 495 nm, slightly lower than the DLS results. This discrepancy arises because DLS measures the hydrodynamic diameter of colloidal particles in water, whereas SEM provides the diameter of dried particles. Typically, the solvation layer is dense, and nanoparticles tend to aggregate, resulting in a larger hydrodynamic dimension measured by DLS in aqueous suspension.[80]

4. INVESTIGATION INTO THE DRUG'S LOADING AND ENTRAPMENT EFFICIENCY (LE% AND EE%)

The drug demonstrated efficacy ratings of 31% for loading (LE %) and 73% for entrapment (EE%). Notably, the entrapment efficiency in this study was significantly higher than that in previous reports. For instance, Fe_3O_4/SiO_2/HAp and Fe_3O_4/ SiO_2/HAp/APTES had EE% values of 42.4% and 69.6%,[60] respectively. Another study by Narayanan et al.[81] reported an EE% of 40% for chitosan nano-emulsions with attached PTH (1−34).

5. STUDY ON PTH (1−34) RELEASE

Figure 6 presents the results of in vitro PTH (1−34) diffusion over 24 h in normal pH (7.4) and acidic pH (5.6). The choice of acidic pH was based on its better representation of the subcutaneous microenvironment and pH-sensitive evaluation. The release of the drug was higher in an acidic pH (88%) compared to a normal pH (43%) after 24 h. The decrease in pH facilitated the release of the peptide hydrophilic drug from nanocarriers due to reduced carboxyl group ionization. Nanocarriers with pH-responsive reactivity have demonstrated improved biocompatibility and the ability to target acidic
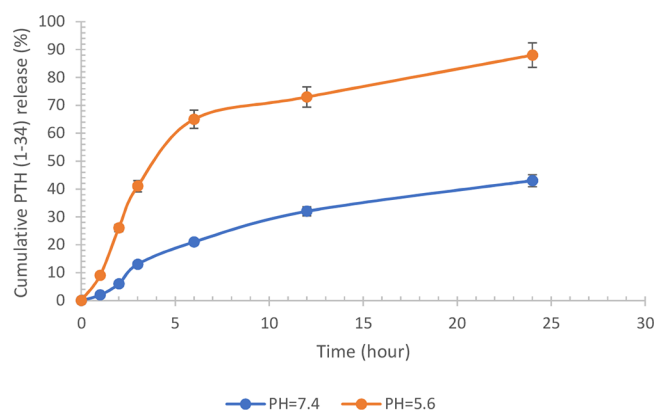

Figure 6. Drug release pattern from the PTH (1−34)-loaded nanocomposite at pH levels of 5.6 and 7.4.

microenvironments, including cancer cells.[82] This study confirmed these capabilities in the fabricated nanocomposite.

6. MTT ASSAY

As shown in Figure 7, the research specimens exhibited no apparent toxic effects on the NIH3T3 and HEK-293 cell lines. The combination of HAp and PTH (1−34) in the free drug (20 μg PTH (1−34)) and PTH (1−34)-loaded nanocarrier samples had a synergistic effect, positively impacting cell proliferation and differentiation. This combination not only showed no toxicity but also enhanced biocompatibility, which increased over a 48-h period. The dosage of 20 μg PTH (1−34) used in this study aligns with the FDA-approved clinical prescriptions,[83] ensuring no concerns regarding reduced cell viability. Therefore, utilization of this drug delivery system is recommended for clinical applications. These findings are consistent with a previous study, which found no cytotoxicity in the MC3T3-E1 cell line after 24 h when analyzing free and PTH-loaded bilayer implants.[84]

7. FINDINGS FROM IN VIVO INVESTIGATION OF DRUG RELEASE

In order to examine the impact of a magnetic field on the conduction of nanodrugs, the quantity of the drug present in rat bone tissue was studied at different time intervals: 2, 5, 10, and 30 min (refer to Table 1). To accomplish this, the bone tissue was extracted from the animal's body at the specified time intervals, and the drug concentration was analyzed using the HPLC analytical technique. A control sample was used for comparison. It is worth noting that to assess the impact and amount of nanodrug entrapment in vital tissues such as the lungs, the drug was administered via arterial injection.

During the investigation of two groups, one with magnetic field and one without, the superparamagnetic properties of the nanocomposite were observed. It was found that the utilization of an external magnetic field significantly increased the release of the drug molecules. Interestingly, the concentration of nanodrugs and conventional drugs in bone tissue did not differ significantly when a magnetic field was not applied. This highlights the importance of the magnetic field's effect and the magneto-responsive nature of the nanocomposite. Additionally, lung lavage was performed, and the amount of drug in it was checked, which was very low that confirmed the effectiveness of nano medicine by magnetic field.
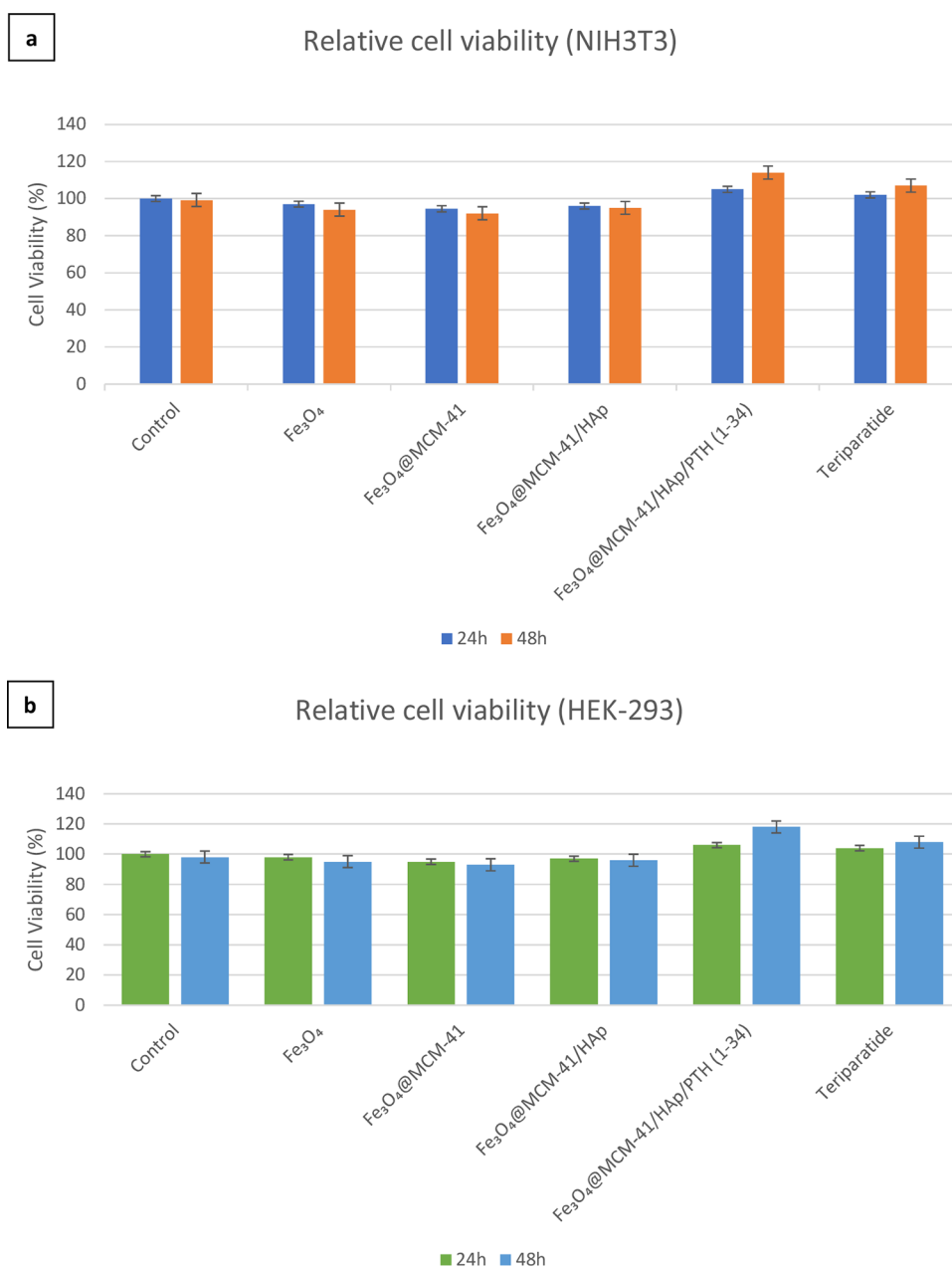
Figure 7. MTT assay and cytotoxicity analysis of free PTH (1−34) and 4 sample nanocarriers (compared with control cells) used; (a) NIH3T3 cell line and (b) HEK-293 cell line

Table 1. Release Concentration of Teriparatide at 2, 5, 10, and 30 after the In Vitro Test

time (min)	2	5	10	30
mean concentration in the bone tissue of the first group (μg)	107	190	378	505
mean concentration in the bone tissue of the second group (μg)	5	15	24	69

8. CONCLUSIONS

Fractures and bone-related illnesses affect a significant portion of the population. Although several protein-based medications have been approved, their use can result in substantial adverse effects and high costs. The development of a drug-carrying nanocomposite, as demonstrated in this study, allows for localized drug delivery. The choice between systemic or local treatment depends on the clinical condition and the require-

ments of the patient. Alternatively, a combination approach can be employed, where a localized depot is inserted at the site of injury to expedite the early stages of healing followed by systemic therapy to enhance bone production and mineralization.

The combination of Fe_3O_4 NPs and mesoporous materials presents numerous possibilities for tailoring the material to various applications, including hydrophilic and hydrophobic drug-carrying therapies utilizing magnetic targeting as well as selective drug extraction from complex biological environments. This combination offers high drug loading capacity and a narrow pore size distribution. Through further analyses, Fe_3O_4@MCM-41/HAp/PTH (1−34) has been successfully synthesized as an advanced biocompatible drug delivery system. Studies have demonstrated that these integrated drug delivery systems can modify the biodistribution of treatments,

enhance the therapeutic effect of bone formation, reduce systemic side effects of drugs, prolong drug half-lives, and improve bioavailability. Another advantage of this method is the ability to achieve high drug density on the nanocomposite, with the capability to control long-term drug delivery.

■ ASSOCIATED CONTENT

Data Availability Statement

Data and materials may be obtained via the corresponding author upon request.

ⓈⒾ Supporting Information

The Supporting Information is available free of charge at https://pubs.acs.org/doi/10.1021/acsomega.3c04931.

> The HPLC peak of the drug in 2, 5, 10 and 30 min after release, with the peak in the 4.5 min bill related to the drug (PDF)

■ AUTHOR INFORMATION

Corresponding Author

Majid Abdouss − *Department of Chemistry, Amirkabir University of Technology, Tehran 1591634311, Iran;* Ⓞ orcid.org/0000-0003-2305-7985; Email: phdabdouss44@aut.ac.ir

Authors

Hamid Reza Hosseini − *Department of Biomedical Engineering, Central Tehran Branch, Islamic Azad University, Tehran 13185/768, Iran;* Ⓞ orcid.org/0000-0002-1118-5819

Mostafa Golshekan − *Guilan Road Trauma Research Center, Guilan University of Medical Sciences, Rasht 13111-41937, Iran*

Complete contact information is available at:
https://pubs.acs.org/10.1021/acsomega.3c04931

Author Contributions

H.R.H.: Data curation, frontiers research, resources, investigation, writing an original draft, laboratory syntheses, conducting required analyses and tests, writing- review and editing, in vivo test. M.A.: Conceptualization, Validation, Investigation, Supervision. M.G.: Methodology, Formal analysis, In vivo test.

Notes

The authors declare no competing financial interest.
Approval id: IR.IAU.REC.1401.034 from the research ethics committee's certificate.
All authors have given their consent for publication.

■ ACKNOWLEDGMENTS

■ REFERENCES

(1) Melton, L. J.; Achenbach, S. J.; Atkinson, E. J.; Therneau, T. M.; Amin, S. Long-term mortality following fractures at different skeletal sites: a population-based cohort study. *Osteoporosis Int.* **2013**, *24* (5), 1689−1696.

(2) Somersalo, A.; Paloneva, J.; Kautiainen, H.; Lönnroos, E.; Heinänen, M.; Kiviranta, I. Increased mortality after upper extremity fracture requiring inpatient care. *Acta Orthop.* **2015**, *86* (5), 533−557.

(3) Somersalo, A.; Paloneva, J.; Kautiainen, H.; LÖNnroos, E.; HeinÄNen, M.; Kiviranta, I. Increased mortality after lower extremity fractures in patients < 65 years of age. *Acta Orthop.* **2016**, *87* (6), 622−625.

(4) Albrecht, B. M.; Stalling, I.; Foettinger, L.; Recke, C.; Bammann, K. Adherence to Lifestyle Recommendations for Bone Health in Older Adults with and without Osteoporosis: Cross-Sectional Results of the OUTDOOR ACTIVE Study. *Nutrients* **2022**, *14* (12), 2463.

(5) Jones, M. S.; Waterson, B. Principles of management of long bone fractures and fracture healing. *Surgery* **2020**, *38* (2), 91−99.

(6) Chen, J.; Ashames, A.; Buabeid, M. A.; Fahelelbom, K. M.; Ijaz, M.; Murtaza, G. Nanocomposites drug delivery systems for the healing of bone fractures. *Int. J. Pharm.* **2020**, *585*, No. 119477.

(7) Cometa, S.; Bonifacio, M. A.; Tranquillo, E.; Gloria, A.; Domingos, M.; De Giglio, E. A 3D Printed Composite Scaffold Loaded with Clodronate to Regenerate Osteoporotic Bone. *In Vitro Charact. Polym.* **2021**, *13* (1), 150.

(8) Russo, T.; De Santis, R.; Peluso, V.; Gloria, A., Multifunctional Bioactive Magnetic Scaffolds with Tailored Features for Bone Tissue Engineering. In *Magnetic Nanoparticles in Human Health and Medicine*; 2021; pp 87−112.

(9) Pavlychuk, T.; Chernogorskyi, D.; Chepurnyi, Y.; Neff, A.; Kopchak, A. Application of CAD/CAM technology for surgical treatment of condylar head fractures: A preliminary study. *J. Oral Biol. Craniofacial Res.* **2020**, *10* (4), 608−614.

(10) Momesso, G. A. C.; Polo, T. O. B.; da Silva, W. P. P.; Barbosa, S.; Freitas, G. P.; Lopes, H. B.; Rosa, A. L.; Cordeiro, J. M.; Toro, L. F.; Chiba, F. Y.; Matsushita, D. H.; Louzada, M. J. Q.; da Cruz, N. C.; Barão, V. A. R.; Faverani, L. P. Miniplates coated by plasma electrolytic oxidation improve bone healing of simulated femoral fractures on low bone mineral density rats. *Mater. Sci. Eng.: C* **2021**, *120*, No. 111775.

(11) Wang, C.-J.; Chen, H.-S.; Chen, C.-E.; Yang, K. D. Treatment of Nonunions of Long Bone Fractures With Shock Waves. *Clin. Orthop. Relat. Res.* **2001**, *387*, 95−101.

(12) Kumar, R.; Sarkar, C.; Panja, S.; Khatua, C.; Gugulothu, K.; Sil, D., Biomimetic Nanocomposites for Biomedical Applications. In *Biorenewable Nanocomposite Materials, Vol. 1: Electrocatalysts and Energy Storage*; American Chemical Society: 2022; Vol. *1410*, pp 163−196.

(13) Kim, T.; See, C. W.; Li, X.; Zhu, D. Orthopedic implants and devices for bone fractures and defects: Past, present and perspective. *Eng. Regener.* **2020**, *1*, 6−18.

(14) Bahari Javan, N.; Rezaie Shirmard, L.; Jafary Omid, N.; Akbari Javar, H.; Rafiee Tehrani, M.; Abedin Dorkoosh, F. Preparation, statistical optimization and in vitro characterisation of poly (3-hydroxybutyrate-co-3-hydroxyvalerate)/poly (lactic-co-glycolic acid) blend nanoparticles for prolonged delivery of teriparatide. *J. Microencapsulation* **2016**, *33* (5), 460−474.

(15) Kim, S.-J.; Park, H.-S.; Lee, D.-W.; Lee, J.-W. Short-term daily teriparatide improve postoperative functional outcome and fracture healing in unstable intertrochanteric fractures. *Injury* **2019**, *50* (7), 1364−1370.

(16) Khosla, S.; Hofbauer, L. C. Osteoporosis treatment: recent developments and ongoing challenges. *Lancet Diabetes Endocrinol.* **2017**, *5* (11), 898−907.

(17) Amani, N.; Javar, H. A.; Dorkoosh, F. A.; Rouini, M. R.; Amini, M.; Sharifzadeh, M.; Boumi, S. Preparation and Pulsatile Release Evaluation of Teriparatide-Loaded Multilayer Implant Composed of Polyanhydride-Hydrogel Layers Using Spin Coating for the Treatment of Osteoporosis. *J. Pharm. Innovation* **2021**, *16* (2), 337−358.

(18) Trevisani, V. F. M.; Riera, R.; Imoto, A. M.; Saconato, H.; Atallah, Á. N. Teriparatide (recombinant human parathyroid hormone 1−34) in postmenopausal women with osteoporosis: systematic review. *Sao Paulo Med. J.* **2008**, *126* (5), 279−284.

(19) Sowa, H.; Hamaya, E.; Yamamoto, T. Teriparatide: human recombinant parathyroid hormone (1−34) as a daily subcutaneous injection. *Clin. Calcium* **2011**, *21* (1), 9−16.

(20) Buckley, L.; Guyatt, G.; Fink, H. A.; Cannon, M.; Grossman, J.; Hansen, K. E.; Humphrey, M. B.; Lane, N. E.; Magrey, M.; Miller, M. 2017 American College of Rheumatology guideline for the prevention and treatment of glucocorticoid-Induced osteoporosis. *Arthritis Rheumatol.* **2017**, *69* (8), 1521−1537.

(21) Gilsenan, A.; Harding, A.; Kellier-Steele, N.; Harris, D.; Midkiff, K.; Andrews, E. The Forteo Patient Registry linkage to multiple state cancer registries: study design and results from the first 8 years. *Osteoporosis Int.* **2018**, *29* (10), 2335−2343.

(22) HIGHLIGHTS OF PRESCRIBING INFORMATION These highlights do not include all the information needed to use FORTEO safely and effectively. See full prescribing information for FORTEO. Company, E. L. A., Ed. 2020.

(23) Cengiz, B.; Gokce, Y.; Yildiz, N.; Aktas, Z.; Calimli, A. Synthesis and characterization of hydroxyapatite nanoparticles. *Colloids Surf., A* **2008**, *322* (1), 29−33.

(24) Lee, H. J.; Kim, S. E.; Choi, H. W.; Kim, C. W.; Kim, K. J.; Lee, S. C. The effect of surface-modified nano-hydroxyapatite on biocompatibility of poly(ε-caprolactone)/hydroxyapatite nanocomposites. *Eur. Polym. J.* **2007**, *43* (5), 1602−1608.

(25) Abdul Halim, N. A.; Hussein, M. Z.; Kandar, M. K. Nanomaterials-upconverted hydroxyapatite for bone tissue engineering and a platform for drug delivery. *Int. J. Nanomed.* **2021**, 6477−6496.

(26) Mondal, S. K.; Dorozhkin, S. V.; Pal, U. Recent progress on fabrication and drug delivery applications of nanostructured hydroxyapatite. *Wiley Interdiscip. Rev.: Nanomed. Nanobiotechnol.* **2018**, *10* (4), No. e1504.

(27) Aghaei, H.; Nourbakhsh, A. A.; Karbasi, S.; JavadKalbasi, R.; Rafienia, M.; Nourbakhsh, N.; Bonakdar, S.; Mackenzie, K. J. D. Investigation on bioactivity and cytotoxicity of mesoporous nanocomposite MCM-48/hydroxyapatite for ibuprofen drug delivery. *Ceram. Int.* **2014**, *40* (5), 7355−7362.

(28) Kundu, B.; Ghosh, D.; Sinha, M. K.; Sen, P. S.; Balla, V. K.; Das, N.; Basu, D. Doxorubicin-intercalated nano-hydroxyapatite drug-delivery system for liver cancer: An animal model. *Ceram. Int.* **2013**, *39* (8), 9557−9566.

(29) Thomas, S. C.; Kumar Mishra, P.; Talegaonkar, S. Ceramic nanoparticles: fabrication methods and applications in drug delivery. *Curr. Pharm. Des.* **2015**, *21* (42), 6165−6188.

(30) Habraken, W.; Habibovic, P.; Epple, M.; Bohner, M. Calcium phosphates in biomedical applications: materials for the future? *Mater. Today* **2016**, *19* (2), 69−87.

(31) Chahkandi, M.; Mirzaei, M. Structural and particle size evolution of sol−gel-derived nanocrystalline hydroxyapatite. *J. Iran. Chem. Soc.* **2017**, *14* (3), 567−575.

(32) Mahmoudi, M.; Sant, S.; Wang, B.; Laurent, S.; Sen, T. Superparamagnetic iron oxide nanoparticles (SPIONs): Development, surface modification and applications in chemotherapy. *Adv. Drug Delivery Rev.* **2011**, *63* (1), 24−46.

(33) Mohapatra, M.; Anand, S. Synthesis and applications of nanostructured iron oxides/hydroxides−a review. *Int. J. Eng., Sci. Technol.* **2011**, *2* (8), 63846.

(34) Leslie-Pelecky, D. L.; Rieke, R. D. Magnetic properties of nanostructured materials. *Chem. Mater.* **1996**, *8* (8), 1770−1783.

(35) Wei, Y.; Han, B.; Hu, X.; Lin, Y.; Wang, X.; Deng, X. Synthesis of Fe_3O_4 Nanoparticles and their Magnetic Properties. *Procedia Eng.* **2012**, *27*, 632−637.

(36) Hosseini, S. M.; Abdouss, M.; Mazinani, S.; Soltanabadi, A.; Kalaee, M. Modified nanofiber containing chitosan and graphene oxide-magnetite nanoparticles as effective materials for smart wound dressing. *Composites, Part B* **2022**, *231*, No. 109557.

(37) Shuai, C.; Yang, W.; He, C.; Peng, S.; Gao, C.; Yang, Y.; Qi, F.; Feng, P. A magnetic micro-environment in scaffolds for stimulating bone regeneration. *Mater. Des.* **2020**, *185*, No. 108275.

(38) Marycz, K.; Sobierajska, P.; Wiglusz, R.; Idczak, R.; Nedelec, J.-M.; Fal, A.; Kornicka-Garbowska, K. Fe_3O_4 Magnetic Nanoparticles Under Static Magnetic Field Improve Osteogenesis via RUNX-2 and Inhibit Osteoclastogenesis by the Induction of Apoptosis. *Int. J. Nanomed.* **2020**, *15*, 10127−10148.

(39) Faraji, M.; Yamini, Y.; Rezaee, M. Magnetic nanoparticles: synthesis, stabilization, functionalization, characterization, and applications. *J. Iran. Chem. Soc.* **2010**, *7* (1), 1−37.

(40) Ye, X.-R.; Daraio, C.; Wang, C.; Talbot, J.; Jin, S. Room temperature solvent-free synthesis of monodisperse magnetite nanocrystals. *J. Nanosci. Nanotechnol.* **2006**, *6* (3), 852−856.

(41) Mou, X.; Ali, Z.; Li, S.; He, N. Applications of magnetic nanoparticles in targeted drug delivery system. *J. Nanosci. Nanotechnol.* **2015**, *15* (1), 54−62.

(42) Ulu, A.; Noma, S. A. A.; Koytepe, S.; Ates, B. Magnetic Fe3O4@MCM-41 core−shell nanoparticles functionalized with thiol silane for efficient l-asparaginase immobilization. *Artif. Cells, Nanomed., Biotechnol.* **2018**, *46* (sup2), 1035−1045.

(43) Carrillo, A. I.; Serrano, E.; Luque, R.; García-Martínez, J. Microwave-assisted catalysis by iron oxide nanoparticles on MCM-41: Effect of the support morphology. *Appl. Catal., A* **2013**, *453*, 383−390.

(44) Conesa, T. D.; Mokaya, R.; Campelo, J. M.; Romero, A. A. Synthesis and characterization of novel mesoporous aluminosilicate MCM-41 containing aluminophosphate building units. *Chem. Commun.* **2006**, *17*, 1839−1841.

(45) Shadabfar, M.; Abdouss, M.; Khonakdar, H. A. Synthesis, characterization, and evaluation of a magnetic molecular imprinted polymer for 5-fluorouracil as an intelligent drug delivery system for breast cancer treatment. *J. Mater. Sci.* **2020**, *55* (26), 12287−12304.

(46) Pourhasan-Kisomi, R.; Shirini, F.; Golshekan, M. Introduction of organic/inorganic Fe3O4@MCM-41@Zr-piperazine magnetite nanocatalyst for the promotion of the synthesis of tetrahydro-4H-chromene and pyrano[2,3-d]pyrimidinone derivatives. *Appl. Organomet. Chem.* **2018**, *32* (7), No. e4371.

(47) Hartmann, M.; Kostrov, X. Immobilization of enzymes on porous silicas − benefits and challenges. *Chem. Soc. Rev.* **2013**, *42* (15), 6277−6289.

(48) Esmaeilnejad-Ahranjani, P.; Kazemeini, M.; Singh, G.; Arpanaei, A. Amine-functionalized magnetic nanocomposite particles for efficient immobilization of lipase: Effects of functional molecule size on properties of the immobilized lipase. *RSC Adv.* **2015**, *5* (42), 33313−33327.

(49) Babaki, M.; Yousefi, M.; Habibi, Z.; Brask, J.; Mohammadi, M. Preparation of highly reusable biocatalysts by immobilization of lipases on epoxy-functionalized silica for production of biodiesel from canola oil. *Biochem. Eng. J.* **2015**, *101*, 23−31.

(50) Jafarzadeh, A.; Sohrabnezhad, S.; Zanjanchi, M. A.; Arvand, M. Synthesis and characterization of thiol-functionalized MCM-41 nanofibers and its application as photocatalyst. *Microporous Mesoporous Mater.* **2016**, *236*, 109−119.

(51) Popova, T.; Tzankov, B.; Voycheva, C.; Spassova, I.; Kovacheva, D.; Tzankov, S.; Aluani, D.; Tzankova, V.; Lambov, N. Mesoporous silica MCM-41 and HMS as advanced drug delivery carriers for bicalutamide. *J. Drug Delivery Sci. Technol.* **2021**, *62*, No. 102340.

(52) Ambrogi, V.; Perioli, L.; Pagano, C.; Latterini, L.; Marmottini, F.; Ricci, M.; Rossi, C. MCM-41 for furosemide dissolution improvement. *Microporous Mesoporous Mater.* **2012**, *147* (1), 343−349.

(53) Ambrogi, V.; Perioli, L.; Marmottini, F.; Giovagnoli, S.; Esposito, M.; Rossi, C. Improvement of dissolution rate of piroxicam by inclusion into MCM-41 mesoporous silicate. *Eur. J. Pharm. Sci.* **2007**, *32* (3), 216−222.

(54) Asadi, E.; Abdouss, M.; Leblanc, R. M.; Ezzati, N.; Wilson, J. N.; Kordestani, D. Synthesis, characterization and in vivo drug delivery study of a biodegradable nano-structured molecularly imprinted polymer based on cross-linker of fructose. *Polymer* **2016**, *97*, 226−237.

(55) Mueller, P. S.; Parker, C. P.; Larsen, S. C. One-pot synthesis of iron oxide mesoporous silica core/shell nanocomposites. *Microporous Mesoporous Mater.* **2015**, *204*, 173−179.

(56) Popescu, S.; Ardelean, I. L.; Gudovan, D.; Rădulescu, M.; Ficai, D.; Ficai, A.; Vasile, B. Ş.; Andronescu, E. Multifunctional materials such as MCM-41/Fe₃O₄/folic acid as drug delivery system. *Rom. J. Morphol. Embryol.* **2016**, *57* (2), 483−489.

(57) Rao, Z.; Ge, H.; Liu, L.; Zhu, C.; Min, L.; Liu, M.; Fan, L.; Li, D. Carboxymethyl cellulose modified graphene oxide as pH-sensitive drug delivery system. *Int. J. Biol. Macromol.* **2018**, *107*, 1184−1192.

(58) Li, C.; Wang, Q.; Gu, X.; Kang, Y.; Zhang, Y.; Hu, Y.; Li, T.; Jin, H.; Deng, G.; Wang, Q. Porous Se@SiO(2) nanocomposite promotes migration and osteogenic differentiation of rat bone marrow mesenchymal stem cell to accelerate bone fracture healing in a rat model. *Int. J. Nanomed.* **2019**, *14*, 3845−3860.

(59) Erol-Taygun, M.; Unalan, I.; Idris, M. I. B.; Mano, J. F.; Boccaccini, A. R. Bioactive Glass-Polymer Nanocomposites for Bone Tissue Regeneration Applications: A Review. *Adv. Eng. Mater.* **2019**, *21* (8), No. 1900287.

(60) Mortazavi-Derazkola, S.; Salavati-Niasari, M.; Khojasteh, H.; Amiri, O.; Ghoreishi, S. M. Green synthesis of magnetic Fe₃O₄/SiO₂/HAp nanocomposite for atenolol delivery and in vivo toxicity study. *J. Cleaner Prod.* **2017**, *168*, 39−50.

(61) Zhao, C.-X.; Yu, L.; Middelberg, A. P. J. Magnetic mesoporous silica nanoparticles end-capped with hydroxyapatite for pH-responsive drug release. *J. Mater. Chem. B* **2013**, *1* (37), 4828−4833.

(62) Saadatjoo, N.; Golshekan, M.; Shariati, S.; Azizi, P.; Nemati, F. Ultrasound-assisted synthesis of β-amino ketones via a Mannich reaction catalyzed by Fe3O4 magnetite nanoparticles as an efficient, recyclable and heterogeneous catalyst. *Arabian J. Chem.* **2017**, *10*, S735−S741.

(63) Saadatjoo, N.; Golshekan, M.; Shariati, S.; Kefayati, H.; Azizi, P. Organic/inorganic MCM-41 magnetite nanocomposite as a solid acid catalyst for synthesis of benzo[α]xanthenone derivatives. *J. Mol. Catal. A: Chem.* **2013**, *377*, 173−179.

(64) Mahdi Eshaghi, M.; Pourmadadi, M.; Rahdar, A.; Díez-Pascual, A. M. Novel Carboxymethyl Cellulose-Based Hydrogel with Core-Shell Fe₃O₄@SiO₂ Nanoparticles for Quercetin Delivery. *Materials* **2022**, *15* (24), 8711.

(65) Xie, W.; Zang, X. Immobilized lipase on core−shell structured Fe₃O₄−MCM-41 nanocomposites as a magnetically recyclable biocatalyst for interesterification of soybean oil and lard. *Food Chem.* **2016**, *194*, 1283−1292.

(66) Azizi, P.; Golshekan, M.; Shariati, S.; Rahchamani, J. Solid phase extraction of Cu2+, Ni2+, and Co2+ ions by a new magnetic nano-composite: excellent reactivity combined with facile extraction and determination. *Environ. Monit. Assess.* **2015**, *187* (4), 185.

(67) Rane, S. S.; Ajameri, A.; Mody, R.; Padmaja, P. Development and validation of RP-HPLC and RP-UPLC methods for quantification of parathyroid hormones (1−34) in medicinal product formulated with meta-cresol. *J. Pharm. Anal.* **2012**, *2* (2), 136−142.

(68) Wang, H.; Wang, F.; Tao, X.; Cheng, H. Ammonia-containing dimethyl sulfoxide: An improved solvent for the dissolution of formazan crystals in the 3-(4,5-dimethylthiazol-2-yl)-2,5-diphenyl tetrazolium bromide (MTT) assay. *Anal. Biochem.* **2012**, *421* (1), 324−326.

(69) Mortazavi-Derazkola, S.; Salavati-Niasari, M.; Amiri, O.; Abbasi, A. Fabrication and characterization of Fe₃O₄@SiO₂@TiO₂@Ho nanostructures as a novel and highly efficient photocatalyst for degradation of organic pollution. *J. Energy Chem.* **2017**, *26* (1), 17−23.

(70) Abbas, M.; Parvatheeswara Rao, B.; Nazrul Islam, M.; Naga, S. M.; Takahashi, M.; Kim, C. Highly stable- silica encapsulating magnetite nanoparticles (Fe₃O₄/SiO₂) synthesized using single surfactantless- polyol process. *Ceram. Int.* **2014**, *40* (1, Part B), 1379−1385.

(71) Gupta, V. K.; Agarwal, S.; Saleh, T. A. Chromium removal by combining the magnetic properties of iron oxide with adsorption properties of carbon nanotubes. *Water Res.* **2011**, *45* (6), 2207−2212.

(72) Nnadozie, E. C.; Ajibade, P. A. Green synthesis and characterization of magnetite (Fe₃O₄) nanoparticles using Chromolaena odorata root extract for smart nanocomposite. *Mater. Lett.* **2020**, *263*, No. 127145.

(73) Pourhasan-Kisomi, R.; Shirini, F.; Golshekan, M. Fe₃O₄@MCM-41@NH-SO₃H: an Efficient Magnetically Reusable Nano-Catalyst for the Formylation of Amines and Alcohols. *Silicon* **2022**, *14* (6), 2583−2594.

(74) Li, S.; Yu, W.; Zhang, W.; Zhang, G.; Yu, L.; Lu, E. Evaluation of highly carbonated hydroxyapatite bioceramic implant coatings with hierarchical micro-/nanorod topography optimized for osseointegration. *Int. J. Nanomed.* **2018**, *13*, 3643−3659.

(75) Moradi, S.; Najjar, R.; Hamishehkar, H.; Lotfi, A. Triple-responsive drug nanocarrier: Magnetic core-shell nanoparticles of Fe₃O₄@poly(N-isopropylacrylamide)-grafted-chitosan, synthesis and in vitro cytotoxicity evaluation against human lung and breast cancer cells. *J. Drug Delivery Sci. Technol.* **2022**, *72*, No. 103426.

(76) Rajabzadeh-Khosroshahi, M.; Pourmadadi, M.; Yazdian, F.; Rashedi, H.; Navaei-Nigjeh, M.; Rasekh, B. Chitosan/agarose/graphitic carbon nitride nanocomposite as an efficient pH-sensitive drug delivery system for anticancer curcumin releasing. *J. Drug Delivery Sci. Technol.* **2022**, *74*, No. 103443.

(77) Joseph, E.; Singhvi, G., Chapter 4 - Multifunctional nanocrystals for cancer therapy: a potential nanocarrier. In *Nanomaterials for Drug Delivery and Therapy*; Grumezescu, A. M., Ed.; William Andrew Publishing: 2019; pp 91−116.

(78) Mohebali, A.; Abdouss, M.; Afshar Taromi, F. Fabrication of biocompatible antibacterial nanowafers based on HNT/PVA nanocomposites loaded with minocycline for burn wound dressing. *Mater. Sci. Eng.: C* **2020**, *110*, No. 110685.

(79) Abdollahi, E.; Khalafi-Nezhad, A.; Mohammadi, A.; Abdouss, M.; Salami-Kalajahi, M. Synthesis of new molecularly imprinted polymer via reversible addition fragmentation transfer polymerization as a drug delivery system. *Polymer* **2018**, *143*, 245−257.

(80) Khoee, S.; Shagholani, H.; Abedini, N. Synthesis of quasi-spherical and square shaped oligoamino-ester graft-from magnetite nanoparticles: Effect of morphology and chemical structure on protein interactions. *Polymer* **2015**, *56*, 207−217.

(81) Narayanan, D.; Anitha, A.; Jayakumar, R.; Nair, S. V.; Chennazhi, K. P. Synthesis, Characterization and Preliminary In Vitro Evaluation of PTH 1−34 Loaded Chitosan Nanoparticles for Osteoporosis. *J. Biomed. Nanotechnol.* **2012**, *8* (1), 98−106.

(82) Samadi, A.; Pourmadadi, M.; Yazdian, F.; Rashedi, H.; Navaei-Nigjeh, M.; Eufrasio-da-silva, T. Ameliorating quercetin constraints in cancer therapy with pH-responsive agarose-polyvinylpyrrolidone -hydroxyapatite nanocomposite encapsulated in double nanoemulsion. *Int. J. Biol. Macromol.* **2021**, *182*, 11−25.

(83) United States Pharmacopeial Convention. 2017. *The United States Pharmacopeia 2018: Usp 41; the National Formulary: Nf 36 Official from May 1 2018 ed.*; Rockville MD: United States Pharmacopeial Convention. 41 ed.; 2018.

(84) Eswaramoorthy, R.; Chang, C.-C.; Wu, S.-C.; Wang, G.-J.; Chang, J.-K.; Ho, M.-L. Sustained release of PTH(1−34) from PLGA microspheres suppresses osteoarthritis progression in rats. *Acta Biomater.* **2012**, *8* (6), 2254−2262.